Journal of Computational Physics **155,** 287–306 (1999)
Article ID jcph.1999.6333, available online at http://www.idealibrary.com on IDEAL®

Spectral Collocation Time-Domain Modeling of Diffractive Optical Elements

J. S. Hesthaven,* P. G. Dinesen,† and J. P. Lynov†

*Division of Applied Mathematics, Brown University, Box F, Providence, Rhode Island, 02912; †Department of Optics and Fluid Dynamics, Risø National Laboratory, P.O. Box 49, DK-4000 Roskilde, Denmark
E-mail: jansh@cfm.brown.edu, palle.dinesen@risoe.dk, jens-peter.lynov@risoe.dk

Received December 9, 1998; revised June 9, 1999

A spectral collocation multi-domain scheme is developed for the accurate and efficient time-domain solution of Maxwell's equations within multi-layered diffractive optical elements. Special attention is being paid to the modeling of out-of-plane waveguide couplers. Emphasis is given to the proper construction of high-order schemes with the ability to handle very general problems of considerable geometric and material complexity. Central questions regarding efficient absorbing boundary conditions and time-stepping issues are also addressed. The efficacy of the overall scheme for the time-domain modeling of electrically large, and computationally challenging, problems is illustrated by solving a number of plane as well as non-plane waveguide problems.

Key Words: spectral collocation methods; multi-domain methods; computational electromagnetics; optical elements.

1. INTRODUCTION

Diffractive optical elements (DOEs) comprising surface-relief gratings on thin film optical waveguides have become increasingly interesting for sensor applications as the fabrication technology for such devices has matured [22, 11].

A remaining challenge in the design of DOEs is to specify a surface-relief grating which will produce a desired free-space farfield pattern. A first step in this inverse design process is to solve the forward problem, i.e., to accurately determine the field pattern from a given relief profile. To that end analytic tools are not an option as they are limited to treating periodic structures of infinite extent. What is needed is a tool that allows for the analysis of devices of finite length with chirped, hence aperiodic, surface reliefs.

An alternative to analytic methods is low-order numerical methods such as the finite difference time-domain method (FD-TD). While this approach is fairly straightforward it will in many cases lead to inaccurate results due to the inability to correctly reproduce the

0021-9991/99 $30.00

phase behaviour of the waves [21]. A FD-TD study by Dridi and Bjarklev [6] indicates that a resolution of more than 40 points per wavelength is needed in the analysis of a 10λ long grating coupler using a second-order scheme. Even with a very high resolution, i.e., many points per wavelength, low-order methods will fail to model the phase velocity of the electromagnetic field correctly and, as the DOEs in concern will typically be hundreds of wavelengths long and their functionality critically dependent on the phase of the waves, such phase errors will lead to incorrect results for the fields coupled to free-space. Moreover, to accurately model the details of the interaction between the incoming guided wave and the modulated surface relief, a very accurate description of the relief is required. In the FD-TD method, interfaces are traditionally approximated through a staircase approximation which, in the present case, results in very severe restrictions on the accuracy of the method unless an unrealistic number of grid points are used which, on the other hand, results in very significant memory requirements hence limiting the electric size of the problem.

The need to accurately model the phase behaviour in electrically large structures thus suggests that higher-order methods should be considered. Indeed, as has recently been shown, this is not only an option but a necessity for problems involving electromagnetic scattering by electrically large objects [23].

In this paper, we develop a spectral collocation multi-domain scheme suitable for the modeling of general guided wave problems with an emphasis being put on out-of-plane waveguide couplers as sketched in Fig. 1. The scheme employs a multi-domain Chebyshev collocation method in combination with a curvilinear representation and a smooth mapping, hence providing the necessary geometric flexibility of the computational setting. However, the multi-domain framework not only ensures the geometric flexibility of the scheme but also eases the computational burden associated with traditional one-domain collocation methods while supplying a very natural data-decomposition suitable for efficient implementations on a parallel platform.

The remainder of this paper is organized as follows. In Section 2, the physical picture and Maxwell's equations are outlined. Section 3 discusses the elements of the numerical scheme employed and the performance of the complete framework is addressed in Section 4 through a number of test cases. Concluding remarks are finally given in Section 5.

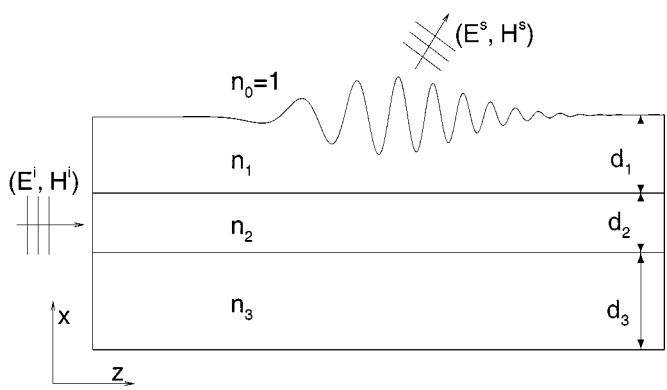

FIG. 1. Typical configuration of a multi-layer diffractive optical element.

2. THE PHYSICAL PICTURE

Although the computational framework developed here is applicable for the modeling of a variety of waveguide phenomena, we shall focus the attention on waveguide grating couplers, i.e., elements in which the electromagnetic energy may be exchanged between guided waves and free space. The forward scattering problem, as shown in Fig. 1, is the subject of main interest here. The modulation of the element/free-space interface manipulates the guided wave and allows for a coupling of waveguide energy into free-space. The actual amplitude and phase modification of the scattered fields depends critically on the details of the modulation of the waveguide surface, hence placing severe constraints on the properties of the numerical scheme.

A typical waveguide grating coupler consists of a number of layers of dielectric material and we shall subsequently assume that all materials can be considered lossless, homogeneous, and non-magnetic. For the guided wave to exist we must assume that the refractive indices of the cladding and the substrate, n_1, and n_3, respectively, must be lower than the refractive index of the core, n_2. The width of the waveguide core, d_2, determines whether the waveguide is a single- or a multi-mode waveguide while the width of the cladding, d_1, is directly related to the amount of coupling between the waveguide and free-space. The width, d_3, of the bulk material with refractive index n_3 is assumed to be sufficiently large that the evanescent waves are undisturbed by the lower edge of the element.

We shall restrict our attention to the two-dimensional transverse electrical (TE) case with the dynamics of the fields being described by Maxwell's equations in the form

$$\begin{aligned}
\frac{\partial \tilde{H}_z}{\partial \tilde{t}} &= -\frac{c}{Z_0}\frac{\partial \tilde{E}_y}{\partial \tilde{x}}, \\
\frac{\partial \tilde{H}_x}{\partial \tilde{t}} &= \frac{c}{Z_0}\frac{\partial \tilde{E}_y}{\partial \tilde{z}}, \\
\frac{\partial \tilde{E}_y}{\partial \tilde{t}} &= cZ_0\frac{1}{n^2}\left(\frac{\partial \tilde{H}_x}{\partial \tilde{z}} - \frac{\partial \tilde{H}_z}{\partial \tilde{x}}\right),
\end{aligned} \tag{1}$$

where $\tilde{H}_z$ and $\tilde{H}_x$ represent the dimensional magnetic fields in the plane while $\tilde{E}_y$ refers to the perpendicular component of the electric field. We have also introduced the free-space impedance, $Z_0 = \sqrt{\mu_0/\varepsilon_0}$, and the vacuum speed of light, $c = 1/\sqrt{\varepsilon_0\mu_0}$, where ε_0 and μ_0 represent the free-space permitivity and permeability, respectively. The index of refraction, $n(z, x)$, is related to the relative permitivity of the dielectric material as $\varepsilon = \varepsilon_r\varepsilon_0 = n^2\varepsilon_0$.

Rather than working with the dimensional equations, we find it more convenient to work with the non-dimensional form arrived at by introducing the new variables

$$x = \tilde{x}/\lambda, \qquad y = \tilde{y}/\lambda, \qquad t = c\tilde{t}/\lambda = \tilde{t}\nu.$$

Here λ is the free-space wavelength of an electromagnetic field with frequency ν. The field components are similarly normalized as

$$H_x = \tilde{H}_x, \qquad H_z = \tilde{H}_z, \qquad E_y = Z_0^{-1}\tilde{E}_y,$$

yielding the non-dimensional TE equations

$$\begin{aligned}\frac{\partial H_z}{\partial t} &= -\frac{\partial E_y}{\partial x},\\ \frac{\partial H_x}{\partial t} &= \frac{\partial E_y}{\partial z},\\ \frac{\partial E_y}{\partial t} &= \frac{1}{n^2}\left(\frac{\partial H_x}{\partial z} - \frac{\partial H_z}{\partial x}\right),\end{aligned} \tag{2}$$

which we shall consider in what remains.

As the materials are considered to be non-magnetic and lossless the field components, H_z, H_x, and E_y, are subject to the boundary conditions

$$E_y^1 = E_y^2, \qquad \hat{\boldsymbol{n}} \times \boldsymbol{H}^1 = \hat{\boldsymbol{n}} \times \boldsymbol{H}^2, \qquad \hat{\boldsymbol{n}} \cdot \boldsymbol{H}^1 = \hat{\boldsymbol{n}} \cdot \boldsymbol{H}^2, \tag{3}$$

where the superscripts refer to the field components in two neighbouring layers while $\hat{\boldsymbol{n}}$ signifies the unit vector normal to the interface. Hence, all field components can be considered continuous, albeit not smooth, for this particular case.

In a typical scenario, the diffractive element is integrated with a laser such that the incoming field is being fed to the element as a guided wave in a multi-layer plane waveguide. As the incoming field we therefore use the fundamental mode of the unperturbed thin film waveguide which may easily be found by semi-analytic means; see, e.g., [18].

3. THE NUMERICAL SCHEME

The construction of the spectral collocation multi-domain scheme for the time-domain solution of Maxwell's equations within a general diffractive optical element involves the combination of a number of techniques. In the following we shall discuss in some detail the individual elements of and the reasoning behind the complete multi-domain scheme for the solution of Eq. (2) subject to the prescribed initial and boundary conditions.

3.1. *Chebyshev Spectral Methods*

The scheme is based on a Chebyshev collocation method. Due to their superior approximation properties, these methods are widely used for the solution of partial differential equations [17].

The Chebyshev polynomial of order k is defined as

$$T_k(z) = \cos(k \cos^{-1} z),$$

where $|z| \leq 1$. We will consider collocation methods, where the $M+1$ collocation points are chosen to be the Chebyshev–Gauss–Lobatto points appearing as the roots of the polynomial $(1-z^2)T'_M(z)$, i.e.,

$$z_i = -\cos\left(\frac{i\pi}{M}\right), \qquad 0 \leq i \leq M.$$

When applying a Chebyshev collocation method the function, $f(z)$, is approximated by a grid function, $f_i = f(z_i)$ where the grid-points are the Gauss–Lobatto points. We construct

a global Mth order Chebyshev interpolant, I_M, to obtain the approximation of the function

$$(I_M f)(z) = \sum_{i=0}^{M} f_i g_i(z),$$

where the interpolating Chebyshev–Lagrange polynomials are given as

$$g_i(z) = \frac{(1-z^2)T'_M(z)(-1)^{i+1}}{c_i M^2 (z - z_i)},$$

where $c_0 = c_M = 2$ and $c_i = 1$ for $1 \le i \le M-1$.

To seek approximate solutions, $(I_M f)(z)$, to a partial differential equation we ask that the equation is satisfied in a collocation sense, i.e., at the collocation points. Hence, we need to obtain values of the spatial derivatives at the collocation points. This is accomplished by approximating the continuous differential operator by a matrix operator with the entries given as

$$D_{ij} = g'_j(z_i),$$

such that the derivative of f at a collocation point, z_i, is approximated as

$$\frac{df}{dz}(z_i) \approx \frac{d(I_M f)}{dz}(z_i) = \sum_{j=0}^{N} D_{ij} f(z_j),$$

and likewise for higher derivatives. For the explicit expressions of the entries of the matrix operator and further details on collocation methods, we refer to [8].

The extension of this one-dimensional framework to a multi-dimensional setting is most easily accomplished through the use of tensor products; e.g., given the function, $f(z, x)$, we construct the two-dimensional approximation

$$(I_{M,N} f)(z, x) = \sum_{i=0}^{M} \sum_{j=0}^{N} f(z_i, x_j) g_i(z) g_j(x),$$

where we have introduced the Chebyshev–Gauss–Lobatto grid, x_j, along x (see Fig. 1). The advantage of this approach lies in the computation of derivatives through the use of one-dimensional differentiation matrices and matrix–matrix products. However, the use of tensor products also requires that $f(z, x)$ is defined on a rectangular grid, a restriction that we shall overcome shortly by introducing a curvilinear representation.

To increase the robustness of the scheme we find it useful to introduce a very weak filtering of the solution. We employ an exponential filter of the type

$$\sigma_i = \begin{cases} 1, & 0 \le i \le M_c \\ \exp\left[-\alpha \left(\frac{i - M_c}{M - M_c}\right)^{\gamma}\right], & M_c < i \le M, \end{cases} \tag{4}$$

where M_c is a cut-off mode number, γ is the order of the filter, and $\alpha = -\ln \varepsilon_M$ with ε_M being the machine accuracy. The filtering along z may conveniently be expressed as a matrix

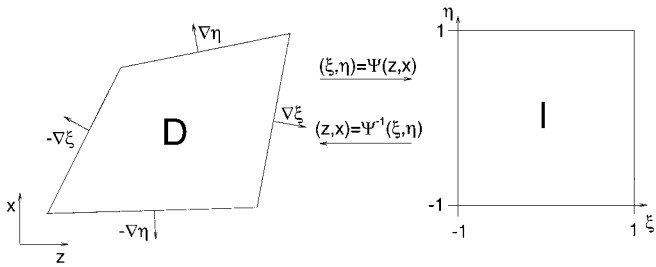

FIG. 2. Illustration of the mapping between physical coordinates, (z, x), and general curvilinear coordinates, (ξ, η), required for the construction of the general multi-domain scheme.

operator, $\mathcal{F}$, with the entries given as

$$\mathcal{F}_{ij} = \frac{2}{c_j M} \sum_{k=0}^{M} \frac{\sigma_k}{c_k} T_k(z_i) T_k(z_j),$$

and likewise for filtering along x.

3.2. *Maxwell's Equations in Curvilinear Form*

The first step towards a geometrically flexible spectral collocation scheme is to extend the use of polynomial expansions to the general curvilinear quadrilateral domain. We assume the existence of a smooth non-singular mapping function, Ψ, relating the (z, x) coordinate system to the general curvilinear coordinate system (ξ, η) as

$$\xi = \xi(z, x), \qquad \eta = \eta(z, x),$$

as illustrated in Fig. 2. We shall return to the actual specification and construction of the smooth map, Ψ, shortly.

Adapting this formulation for Eq. (2) yields the hyperbolic system

$$\frac{\partial \boldsymbol{q}}{\partial t} + \mathrm{A}(\nabla\xi)\frac{\partial \boldsymbol{q}}{\partial \xi} + \mathrm{A}(\nabla\eta)\frac{\partial \boldsymbol{q}}{\partial \eta} = 0, \tag{5}$$

where we have the state vector, $\boldsymbol{q} = (H_z, H_x, E_y)^T$. The general operator, $\mathrm{A}(\boldsymbol{m})$, in which $\boldsymbol{m} = (m_z, m_x)$ represents the local metric, is given as

$$\mathrm{A}(\boldsymbol{m}) = \begin{bmatrix} 0 & 0 & n_x \\ 0 & 0 & -n_z \\ m_x n^{-2} & -m_z n^{-2} & 0 \end{bmatrix}, \tag{6}$$

where we recall that the scalar n refers to the local index of refraction. Locally, this operator diagonalizes under the similarity transform, $\mathrm{A}(\boldsymbol{m}) = \mathrm{S}^{-1}(\boldsymbol{m})\Lambda(\boldsymbol{m})\mathrm{S}(\boldsymbol{m})$, where the diagonal eigenvalue matrix, $\Lambda(\boldsymbol{m})$, has the entries $\Lambda(\boldsymbol{m}) = |\boldsymbol{m}|\mathrm{diag}[-n^{-1}, 0, n^{-1}]$ corresponding to the characteristic velocities of the waves counter-, non-, and co-propagating along the normal vector $\boldsymbol{m}$ with the local speed of light. We recall that $|\boldsymbol{m}|$ represents the length of the vector $\boldsymbol{m}$, such that $\boldsymbol{m} = |\boldsymbol{m}|(\hat{m}_z, \hat{m}_x)$.

The diagonalizing matrices, $\mathrm{S}(\boldsymbol{m})$ and $\mathrm{S}^{-1}(\boldsymbol{m})$, take the form

$$\mathrm{S}(\boldsymbol{m}) = \begin{bmatrix} -\hat{m}_x & \hat{m}_z & -\hat{m}_x \\ \hat{m}_z & \hat{m}_x & \hat{m}_z \\ n^{-1} & 0 & -n^{-1} \end{bmatrix}, \qquad \mathrm{S}^{-1}(\boldsymbol{m}) = \frac{1}{2} \begin{bmatrix} -\hat{m}_x & \hat{m}_z & n \\ 2\hat{m}_z & 2\hat{m}_x & 0 \\ -\hat{m}_x & \hat{m}_z & -n \end{bmatrix},$$

from which we obtain the characteristic variables

$$\boldsymbol{R} = \mathrm{S}^{-1}(\boldsymbol{m})\boldsymbol{q} = \begin{bmatrix} R_1 \\ R_2 \\ R_3 \end{bmatrix} = \frac{1}{2} \begin{bmatrix} -\hat{m}_x H_z + \hat{m}_z H_x + nE_y \\ 2\hat{m}_z H_z + 2\hat{m}_x H_x \\ -\hat{m}_x H_z + \hat{m}_z H_x - nE_y \end{bmatrix}.$$

Aside from revealing information about the dynamics of the fields, the identification and use of the characteristic variables plays, as we shall see shortly, an integral role in the specification of the multi-domain scheme.

3.3. *The Multi-Domain Formulation*

We wish to solve Eq. (5) within a general computational domain, $\Omega \in \mathbf{R}^2$, in the (z, x)-plane. As we have briefly discussed, the most natural and computational efficient way of applying polynomial expansions in several dimensions is through the use of tensor products. This procedure, however, requires that the computational domain can be smoothly mapped to the unit square. To overcome this limitation, we construct Ω using K non-overlapping general curvilinear quadrilaterals, $\mathbf{D}^k \subset \mathbf{R}^2$, such that $\Omega = \bigcup_{k=1}^{K} \mathbf{D}^k$.

The advantages of such an approach, besides from providing the geometric flexibility, are many. In particular in connection with spectral methods, the multi-domain framework results in a lower total operation count and an increased allowable time-step while providing a very natural data-decomposition, well suited for the implementation on contemporary parallel computers as we shall discuss further in Subsection 4.4. We refer to [14, 7, 12] for a thorough discussion of the advantages of using a multi-domain formulation when solving wave-dominated problems.

Once we have split the global computational domain into K sub-domains, we need to construct the map, $\Psi\colon \mathbf{D} \to \mathbf{I}$ (see Fig. 2) where $\mathbf{I} \subset \mathbf{R}^2$ is the unit square, i.e., $\mathbf{I} = [-1, 1]^2$. At this point we have the Cartesian coordinates, $(z, x) \in \mathbf{D}$, and the general curvilinear coordinates, $(\xi, \eta) \in \mathbf{I}$, related through the map, $(x, y) = \Psi(\xi, \eta)$. To establish a one-to-one correspondence between the unit square and the general quadrilateral, we construct the local map for each sub-domain using transfinite blending functions [9]. We refer to [13] for a thorough account of this procedure within the present context. Having constructed the global map, Ψ, we may compute the metric of the mapping and outward pointing normal vectors at all points of the enclosing edges of the quadrilateral.

Within the multi-domain setting we must solve K independent problems in the individual sub-domains. However, to obtain the global solution we must ensure that information is passed between the sub-domains in a way consistent with the dynamics of the Maxwell equations. In the particular scenario considered here, and illustrated in Fig. 1, we encounter two different types of interfaces, requiring different techniques of patching.

The patching across boundaries of domains in regions of different material properties is accomplished by using the physical conditions on the field components, Eq. (3), which are enforced directly.

For the patching of sub-domains of the same material properties we utilize the fact that the system, Eq. (5), is strongly hyperbolic. Hence, it is only natural to transfer information between the various sub-domains using the characteristic variables introduced in the previous section.

The characteristic variables, $\boldsymbol{R}$, are convected along the normal, $\hat{\boldsymbol{n}}$, with a speed given by the diagonal elements of $\Lambda(\boldsymbol{m})$. Hence, once the outward normal vector at every grid point on the enclosing boundary of the sub-domain is known, as it is once the map, Ψ, is constructed, we may uniquely determine for each point on the boundary which characteristics are leaving the sub-domain and which are entering and thus need specification. Indeed, we observe from the eigenvalues of A that while R_3 is always leaving the domain and therefore need no boundary condition, R_1 is always entering the computational domain and requires specification to ensure well-posedness. Thus, R_3, leaving a domain, supplies the sought after boundary conditions for R_1 in the neighbouring domain and conversely for R_1 in the first domain. For the non-propagating R_2 we simply use the average across the interface. Once the characteristic variables have been adjusted, the physical fields are recovered through the relation $\mathrm{S}(\boldsymbol{m})\boldsymbol{R} = \boldsymbol{q}$. This procedure is applied along all interface points, including the vertices where it is done dimension-by-dimension as described in [13]. Using this procedure of patching hyperbolic systems, we arrive at the global solution at each time-step, and as we shall see shortly, it is stable as well as accurate. Moreover, in a parallel setting the communication between the sub-domains involves only nearest neighbor interaction between edges.

3.4. *Illumination and Outer Boundary Conditions*

As we limit the attention to linear materials, it is natural to introduce a scattered field/total field formulation such that the major part of the computation is performed with the total fields and the incoming fields are prescribed along an enclosing contour. Outside of this contour only the scattered fields remains and these now need to be terminated, i.e., we are faced with the long standing problem of finding infinite space solutions on a finite computational domain. The critical issue is how to construct appropriate boundary conditions that prevent outgoing waves from being reflected from the artificial numerical boundaries, as such waves may otherwise interact with the true solution and hence falsify the final result.

The introduction of the perfectly matched layer (PML) methods [3] has spawned significant research into such methods. However, problems related to the lack of strong well-posedness of the original PML equations have been exposed [1] for the two-dimensional PML methods and a number of alternatives have recently appeared in the literature.

In [10] a well-posed PML scheme was introduced and shown to perform well in connection with the spectral collocation multi-domain modeling of scattering. We have chosen to use a slightly modified version of that particular scheme given as

$$
\begin{aligned}
&\frac{\partial H_z}{\partial t} = -\frac{\partial E_y}{\partial x} - 2\sigma_x H_z - \sigma_x P_x - \mu_z H_z,\\
&\frac{\partial H_x}{\partial t} = \frac{\partial E_y}{\partial z} - 2\sigma_z H_x - \sigma_z P_z - \mu_x H_x,\\
&\frac{\partial E_y}{\partial t} = \frac{1}{n^2}\left(\frac{\partial H_x}{\partial z} - \frac{\partial H_z}{\partial x}\right) - \sigma_z' Q_z + \sigma_x' Q_x - \frac{2}{n^2}(\mu_z + \mu_x) E_y, \qquad (7)\\
&\frac{\partial P_z}{\partial t} = \sigma_z H_x - \mu_z P_z, \qquad \frac{\partial Q_z}{\partial t} = -\sigma_z Q_z - n^{-2} H_x - \mu_x Q_z,\\
&\frac{\partial P_x}{\partial t} = \sigma_x H_z - \mu_x P_x, \qquad \frac{\partial Q_x}{\partial t} = -\sigma_x Q_x - n^{-2} H_z - \mu_z Q_x.
\end{aligned}
$$

Note that the additional degrees of freedom, making possible the perfectly matched layer property, are introduced through a number of auxiliary fields, described through additional ordinary differential equations, rather than an unphysical splitting of the electromagnetic fields as in [3].

The modifications of the scheme in Eq. (7), as compared to the original scheme in [10], lie in the adaptation to general dielectric media and, more significantly, a stabilization of the scheme through the addition of the terms associated with μ_z and μ_x. This is done to stabilize the unsplit PML scheme when subjected to spatially low frequency fields for which the method is weakly unstable. This latter phenomenon is shared among all time-domain PML methods and is related to a weak instability in the system of ordinary differential equations describing the auxiliary variables. Similar techniques has been exploited to stabilize PML schemes for advective acoustics [2].

The PML assumes a rectangular interface bounded by $|z| \le z_0$ and $|x| \le x_0$ and the absorption profiles takes the polynomial form

$$\sigma_z(z) = C_z(|z| - z_0)^p, \qquad \sigma_x(x) = C_x(|x| - x_0)^p, \tag{8}$$

where the constants, C_z and C_x, are tunable for optimal performance. For simplicity we also take $\mu_z = \sigma_z$ and $\mu_x = \sigma_x$ in Eq. (7) although that need not be so.

In light of the problems associated with using PML methods for spatial low frequency fields, as happens in a significant part of the scattered region due to the very accurate computation of the total fields and little scattering, we have also considered using the matched layer (ML) technique introduced within the context of computational electromagnetics in [23]. This approach involves solving

$$\begin{aligned}
\frac{\partial H_z}{\partial t} &= -\frac{\partial E_y}{\partial x} - (\sigma_z + \sigma_x) H_z, \\
\frac{\partial H_x}{\partial t} &= \frac{\partial E_y}{\partial z} - (\sigma_z + \sigma_x) H_x, \\
\frac{\partial E_y}{\partial t} &= \frac{1}{n^2}\left(\frac{\partial H_x}{\partial z} - \frac{\partial H_z}{\partial x}\right) - \frac{1}{n^2}(\sigma_z + \sigma_x) E_y,
\end{aligned} \tag{9}$$

within the absorbing layers. As for the PML method, the profiles, σ_z and σ_x, are of the form in Eq. (8) within the layer while they vanish outside, i.e., in the total field region. For this method to be comparable in performance to Eq. (7), however, it must be combined with the use of a low-pass filter and a cubic stretching of the grid in the absorbing layer domains—the idea being that as the waves propagate towards the outer boundary they are gradually damped while, on the grid, becoming increasingly high frequency hence enhancing the efficiency of the filter. A more detailed description can be found in [23]. As we shall see shortly, despite its simplicity its performance is comparable to that of the PML scheme except if very high accuracy is required.

3.5. *Issues Related to Time-Stepping*

We advance Maxwell's equations using a low-storage 5-stage 4th order Runge–Kutta scheme developed in [4]. Although it requires an extra step to complete the time step as compared to the standard 4th order Runge–Kutta scheme, it has a slightly larger stability region, ensuring that the total work remains about constant. However, only one storage level is required for the implementation of the scheme.

The time-step, Δt, is chosen to obey the CFL-criteria as

$$\Delta t \leq CFL \times \left(\min_{\Omega} [\sqrt{\chi \cdot \chi}] \right)^{-1},$$

where we have defined the local vector, χ, as a measure of grid-distortion defined as

$$\chi = \left(\frac{|\xi_z|}{\Delta \xi_i} + \frac{|\eta_z|}{\Delta \eta_j}, \frac{|\xi_x|}{\Delta \xi_i} + \frac{|\eta_x|}{\Delta \eta_j} \right),$$

where $\Delta \xi_i$ and $\Delta \eta_j$ refer to the local grid size.

One of the well-known problems associated with the use of spectral collocation methods, as compared to low-order finite difference methods, is the N^{-2}-scaling of the time-step. While one of the advantages of the multi-domain formulation is a significant relaxation of this constraint it remains a problem. In [16] a mapping, having the effect of stretching the grid near the boundaries of the domains with a resulting increased stable Δt, was introduced. The mapping is given as

$$z(\xi) = \frac{\arcsin(\alpha \xi)}{\arcsin \alpha},$$

where ξ refers to the Chebyshev–Gauss–Lobatto grid. The effect of the mapping is to stretch the grid such that for α approaching unity, the grid becomes increasingly equidistant.

However, the mapping is singular and hence introduces an error, ε, that can be controlled by properly specifying α as guided through the relation

$$\varepsilon = \left(\frac{1 - \sqrt{1 - \alpha^2}}{\alpha} \right)^N, \tag{10}$$

yielding a direct relation between α, N, and α. The usual choice of ε is the machine accuracy, i.e., the error introduced by the mapping can be neglected. However, for small values of N this implies that the effect of the stretching is truly marginal [5]. A more natural choice would seem to be that ε be on the order of the error of the approximation [15]. While this leaves the total error unaffected by the mapping, an increased time-step could result.

To come to an understanding of how to specify α under the above reasoning and what effect it has on the Δt, we recall from [16] that choosing

$$\alpha = \cos\left(\frac{\pi}{N} j \right), \tag{11}$$

where j is here some constant, is appropriate for resolving a wave, $\sin(k \pi x)$, with the maximum wavenumber given as

$$k_{\max} = \frac{N}{2} - j, \tag{12}$$

using N grid points in the polynomial expansion, i.e., $j \ll N/2$ measures the number of waves we are willing to sacrifice to increase the overall accuracy. The effect of using Eq. (11) on ε as N increases is seen directly by introducing Eq. (11) into Eq. (10) yielding the result

$$\lim_{N \to \infty} \varepsilon = e^{-j\pi},$$

i.e., fixing j destroys the spectral accuracy of the scheme. Hence, using $j = 1$ as advocated in [19] results in the error being bounded by $e^{-\pi} \simeq 0.04$, thus questioning the value of using a spectral method.

To understand the correct scaling of j with N, let us recall that the leading error of $\sin(k\pi x)$, when approximated with a Chebyshev expansion of order N, is given as

$$\varepsilon_S \simeq \sqrt{\frac{2}{\pi N}} \left(\frac{e\pi k}{2N} \right)^N \leq \left(\frac{e\pi k}{2N} \right)^N. \tag{13}$$

For this to be accurate we must require that

$$\frac{e\pi k}{2N} < 1 \Rightarrow k < \frac{N}{\pi},$$

yielding the well known requirement of π points per wavelength for Chebyshev methods. Using this as a guideline for j in Eq. (12) yields

$$j = \frac{N}{2\pi} \Rightarrow k_{\max} \simeq \frac{N}{\pi}.$$

We immediately see that this choice implies that $\varepsilon \sim \exp(-N/2)$, i.e., the mapping error vanishes at a spectral rate, consistent with the properties of the approximation. We also note that while ε and j vary with N, α becomes a constant since $\alpha = \cos(1/2)$ using Eq. (11).

While this choice of α ensures that the mapping error does not dominate over the approximation error, it is sufficiently different from 0 that an effect on Δt becomes important. Indeed, if we assume that the minimum spacing of the grid is inversely proportional to Δt we obtain the relation

$$\Delta t_{\text{map}} \sim \frac{\alpha}{\sqrt{1-\alpha^2}\arcsin\alpha} \Delta t_{\text{Cheb}},$$

where Δt_{Cheb} represents the time-step associated with the original unmapped Chebyshev–Gauss–Lobatto grid and Δt_{map} is the time-step for the mapped scheme. We note that for $\alpha > 0$, $\Delta t_{\text{map}} > \Delta t_{\text{Cheb}}$. Indeed, for the choice of $\alpha = \cos(1/2)$ we have that $\Delta t_{\text{map}} \simeq 2\Delta t_{\text{Cheb}}$, i.e., the time-step can be doubled without loss of accuracy or stability of the scheme. These results have been confirmed through numerous tests and for marginally resolved problems the use of the mapping is critical in obtaining the expected results.

At first, the above analysis seems to contradict the results of [5] in which it is advocated that α must scale with N to maintain spectral accuracy. In that work, however, ε is always taken as the machine accuracy which is unnecessarily stringent. In the approach advocated above we recall that the error of the mapping scales as $\varepsilon \sim \exp(-N/2)$. Hence, when $\varepsilon \sim \varepsilon_M$, with ε_M being the machine accuracy, the approach suggested in [5] should be followed as that allows for further stretching of the grid as N increases. However, if we take $\varepsilon_M \sim 10^{-16}$ this implies that $N > 75$ which is an irrelevant range for the vast majority of spectral models and certainly for multi-domain schemes.

3.6. *Near- and Farfield Calculations*

As an important postprocessing step, we use a field equivalence principle to facilitate the computation of near- and farfields outside of the computation domain [20].

The basis for a two-dimensional version of the field equivalence principle is the introduction of a virtual contour on which equivalent charge and magnetic current distributions are defined based on the magnetic and electric flux caused by the sources inside the enclosing contour. The fields outside the contour may subsequently be calculated anywhere through a convolution of the equivalent currents with the free-space Green's function.

The field equivalence principle is employed in the frequency domain only, so in general it is necessary to perform a Fourier transformation of the time-domain field components. We are, however, mainly interested in stationary solutions of monochromatic fields obtained after transients have died out. In this case we may directly recover the complex field phasors from the time-domain fields at two times separated by one quarter of a period.

Introducing the equivalent magnetic, $\check{\boldsymbol{J}}_s$, and electric, $\check{\boldsymbol{M}}_s$, currents along the contour with the outward pointing normal vector, $\hat{\boldsymbol{n}}$, as

$$\begin{aligned}\check{\boldsymbol{J}}_s &= \hat{n} \times \check{\boldsymbol{H}}_s,\\ \check{\boldsymbol{M}}_s &= -\hat{n} \times \check{\boldsymbol{E}}_s,\end{aligned}$$

where $\check{\boldsymbol{H}}_s$ and $\check{\boldsymbol{E}}_s$ are the magnetic and electric fields phasors along the virtual contour, one can define a pair of vector potentials as

$$\begin{aligned}\check{\boldsymbol{A}} &= \mu_0 \int_s \check{\boldsymbol{J}}_s G(\boldsymbol{r} \mid \boldsymbol{r}')\, ds\\ \check{\boldsymbol{F}} &= \epsilon_0 \int_s \check{\boldsymbol{M}}_s G(\boldsymbol{r} \mid \boldsymbol{r}')\, ds,\end{aligned}$$

where $\boldsymbol{r}$ is the observation point, $\boldsymbol{r}'$ is the source point, and the integration is taken along the contour.

The two-dimensional free-space Green's function, $G(\boldsymbol{r} \mid \boldsymbol{r}')$, is given as

$$G(\boldsymbol{r} \mid \boldsymbol{r}') = \frac{j}{4} H_0^{(2)}(k|\boldsymbol{r} - \boldsymbol{r}'|),$$

where $H_0^{(2)}$ is the zero-order Hankel function of the second kind, $j = \sqrt{-1}$, and $k = 2\pi/\lambda$ is the wavenumber.

The electric and magnetic fields phasors outside the virtual contour may now be rigorously calculated anywhere through the vector potentials as

$$\begin{aligned}\check{\boldsymbol{E}} &= -j\omega\left(\check{\boldsymbol{A}} + \frac{1}{k^2}\nabla(\nabla \cdot \check{\boldsymbol{A}})\right) - \frac{1}{\epsilon_0}\nabla \times \check{\boldsymbol{F}},\\ \check{\boldsymbol{H}} &= -j\omega\left(\check{\boldsymbol{F}} + \frac{1}{k^2}\nabla(\nabla \cdot \check{\boldsymbol{F}})\right) - \frac{1}{\mu_0}\nabla \times \check{\boldsymbol{A}}.\end{aligned} \tag{14}$$

These equations are valid everywhere and shall be used to compute the nearfield of the surface-relief grating. However, for the computation of the farfield, significant computational simplifications can be made. At first, the Green's function may be approximated as

$$\lim_{k|\boldsymbol{r}-\boldsymbol{r}'|\to\infty} G(\boldsymbol{r} \mid \boldsymbol{r}') = \frac{j^{3/2}}{\sqrt{8\pi k}} \frac{e^{-jk|\boldsymbol{r}-\boldsymbol{r}'|}}{|\boldsymbol{r} - \boldsymbol{r}'|^{1/2}} \simeq \frac{j^{3/2}}{\sqrt{8\pi k}} \frac{e^{-jk(r - r'\cos\psi)}}{r^{1/2}},$$

where $|\boldsymbol{r}-\boldsymbol{r}'|$ is approximated as r for the amplitude factor while the phase term is approximated as $r-r'\cos\psi$ with ψ being the angle between the observation point vector, $\boldsymbol{r}$, and source point vector, $\boldsymbol{r}'$.

Utilizing these farfield approximations, the vector potentials take the form

$$\begin{aligned}\check{\boldsymbol{A}} &\approx \frac{\mu_0 j^{3/2} e^{-jkr}}{\sqrt{8\pi kr}} \int_s \check{\boldsymbol{J}}_s e^{jkr'\cos\psi}\, ds \equiv \frac{\mu_0 j^{3/2} e^{-jkr}}{\sqrt{8\pi kr}} \boldsymbol{N} \\ \check{\boldsymbol{F}} &\approx \frac{\epsilon_0 j^{3/2} e^{-jkr}}{\sqrt{8\pi kr}} \int_s \check{\boldsymbol{M}}_s e^{jkr'\cos\psi}\, ds \equiv \frac{\epsilon_0 j^{3/2} e^{-jkr}}{\sqrt{8\pi kr}} \boldsymbol{L}.\end{aligned} \tag{15}$$

It is clear that in the true farfield limit, it is only necessary to calculate the radiation integrals $\boldsymbol{L}$ and $\boldsymbol{N}$ once for each observation angle, ψ, as the integrals have no explicit dependence on r. The farfield components may subsequently be calculated anywhere by multiplying the observation point dependent distance factors. In contrast, in the nearfield the integration must be performed for every observation point, since the integrals depend directly on the position of the source as well as the observation point.

A note should be made concerning the virtual contour. The calculation based on the free-space Green's function outlined above requires that the enclosing contour be situated in free-space and that it is closed. On the other hand, our problem requires that the waveguide extends to infinity in the direction of propagation to avoid reflections. The virtual contour is therefore restricted to an aperture above the waveguide. As we shall demonstrate the fact that the surface is not closed is of little significance when the aperture is sufficiently wide compared to the modulation of the waveguide surface as the guided wave in the unperturbed waveguide is non-radiating.

4. NUMERICAL EXPERIMENTS

Combining all of the elements described in the previous section into a general computational framework yields a computationally efficient, yet geometrically flexible scheme for the modeling of waveguide phenomena. Moreover, the use of high-order schemes in space as well as in time allows for the accurate modeling of electrically large waveguide structures in a reliable and efficient manner.

In the following we shall discuss a number of test cases, validating the general framework and illustrating the prospects for addressing more general types of waveguide problems.

4.1. *The Planar Waveguide Problem*

As a basic test of the overall accuracy of the scheme, we have done a number of computations of the plane waveguide problem. A typical problem is shown in Fig. 3 illustrating a 6λ long waveguide where the core layer has a thickness of $d_2=\lambda$ and an index of refraction $n_2=1.45$, the cladding layers both have $n_1=n_3=1.4$, while the thickness of the top cladding layer is $d_1=\lambda$ and $d_3=4\lambda$. The total field region, in which the computation is conducted, as well as the surrounding scattered field region with the absorbing layers is shown in Fig. 3.

As a first test of the scheme we shall address the conservation of power in the computational domain in order to establish an optimum trade-off between power dissipation as a result of the weak filtering applied at each time step and the robustness of the numerical

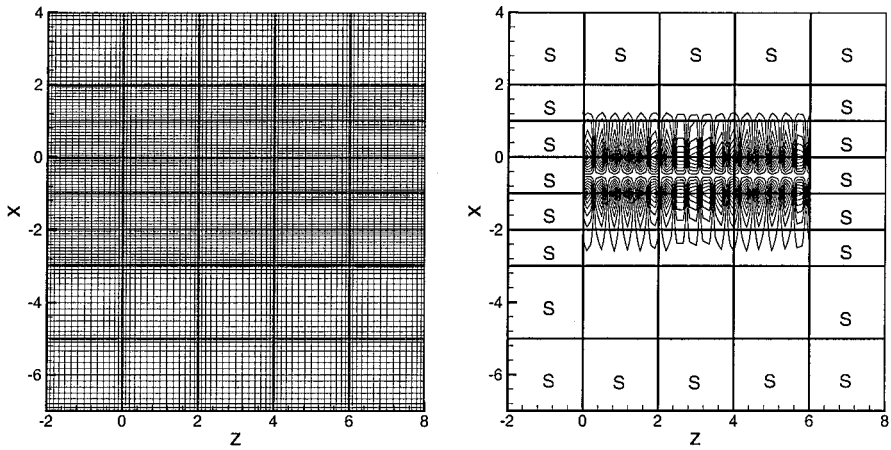

FIG. 3. Illustration of plane waveguide test case. The grid shows the general layout with the high-index waveguide just below $x = 0$ and $N = 16$ modes in each domain. On the right is a snapshot of the H_z component at an arbitrary time illustrating the total field region as well as the surrounding scattered field region (marked by an S).

scheme. We evaluate the power conservation by comparing the power of the incident wave with the output of power below, above, and to the right of the waveguide.

As the initial condition, the exact solution is taken in the entire computational domain, implying that in the PML domains where the scattered field formulation is used, a zero field is initialised. The system is subsequently advanced 10 periods in time. The analysis is performed for a resolution of $M = N = 20$. Table I shows the relative power dissipation for different orders, γ, of the filter, Eq. (4), which is used with $M_c = 0$. We find that increasing the order of the filter beyond 22 renders the algorithm unstable for the given time-step, which corresponds to a CFL number of 3. This unstable behavior can be avoided if the time-step is lowered; however, to reduce the stifness of the algorithm, we choose to apply this very weak filtering. Also, as the wave is guided in the z-direction, the power output perpendicular to the direction of propagation should be negligible as is indeed confirmed by our computations, where we find that the power of the waves propagating through the enclosing upper and lower boundaries are about 11 orders less than the power of the guided wave. In what remains, we shall use a filtering of order 22 which at the same time ensures stability of the scheme with a reasonable time-step and limits the power dissipation to a negligible level.

Looking at the field components after the 10 periods of time advancement we measure the global L_∞ error of the three field components. Table II shows the results, clearly illustrating

TABLE I
Relative Power Dissipation as a Function of the Filtering Order, γ

γ	Relative power loss
12	0.23
16	9.3E-3
20	4.7E-4
22	1.9E-4

TABLE II
Error in the Computation of the Plane Waveguide Solution at $t = 10$

N	N_{ppw}	Δt	$L_\infty(H_z)$	$L_\infty(H_x)$	$L_\infty(E_y)$
12	4.3	3.1E-2	5.0E-2	3.6E-1	2.5E-1
16	5.7	2.1E-2	1.1E-3	8.5E-3	6.0E-3
20	7.1	1.4E-2	6.9E-6	4.8E-5	3.9E-5
24	8.5	1.1E-2	2.2E-6	1.5E-5	1.1E-5

the spectral convergence for increasing number of modes, N, in each sub-domain. One notes in particular that about 7 points per wavelength, N_{ppw}, in the waveguide are sufficient to accurately advance the fields.

4.2. *Absorbing Boundary Layers*

Let us now turn to the issue of designing the absorbing boundary layers for maximum absorption. To investigate this, we temporarily employ a total-field formulation in most of the absorbing layers, however, maintaining the scattered field formulation in the left absorbing layer, to facilitate the continuous feeding of the waveguide at $z = 0$. In this way there is a sufficient amount of energy propagating in the absorbing layers to influence the accuracy of the solution through reflections from the absorbing layers.

Using the grid shown in Fig. 4 with $N = 20$ in each domain it is ensured that the approximation error is small. As a reference solution we use the fields computed on a grid similar to that in Fig. 4, however, extended to $z = 20$. Monitoring the L_∞ error in the domains with $10 < z < 12$ for a time sufficiently short that no reflections can reach these domains, we find the errors to approximately be 5.2E-6, 1.0E-5, and 7.3E-6 for the H_z, H_x, and E_y components, respectively, hence yielding a measure of the pure approximation error. This computation is used in the subsequent analysis rather than the exact solution to remove the effects of the approximation from the evaluation of the performance of the absorbing layers.

A series of calculations has been performed for cases using either the PML scheme, Eq. (7) or the ML scheme, Eq. (9), while varying the thickness of the absorbing layers, L, the order p of the absorption profiles, and the constants C_x and C_z. The best combination

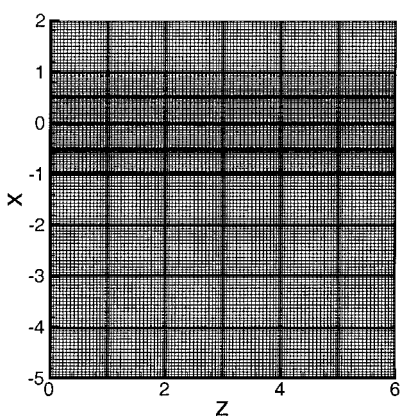

FIG. 4. Grid for waveguide problem testing the efficiency of the absorbing layers.

TABLE III
Optimum Parameters for the Absorbing Layers and the Corresponding Global L_∞ Errors

				L_∞ errors		
Method	p	C	L	H_z	H_x	E_y
ML	4	0.03	2.0	3.6E-5	6.1E-5	5.0E-5
PML	3	0.0275	2.0	5.3E-6	1.9E-5	1.3E-5

for the present problem type in terms of global minimum L_∞ errors are listed in Table III, from which it is found that the PML results in the minimum error, yielding results only slightly above the level of the approximation error. The ML scheme, on the other hand, results in somewhat larger errors, although still acceptable.

4.3. *Out-of-Plane Waveguide Couplers*

Let us now consider a specific example of the generic structure shown in Fig. 1 in more detail. Shown in Fig. 5 is the grid for this test case using $N = 20$ grid points in each domain. The waveguide structure is similar to the above, although the core is slightly thinner with a thickness of $d_2 = 0.8\lambda$. The thickness of the top-cladding layer is 1λ where it is unmodulated and the surface relief is described by the perturbation profile

$$h(z) = A \exp\left(-\left(\frac{z - z_0}{w}\right)^2\right) \sin(2\pi z a_0), \tag{16}$$

where A is the amplitude, z_0 is the center of the modulation, w is the width and a_0 is the inverse modulation period. For the particular case shown in Fig. 5 we have used $A = 0.5$, $z_0 = 10$, $w = 4$, and $a_0 = 0.5$.

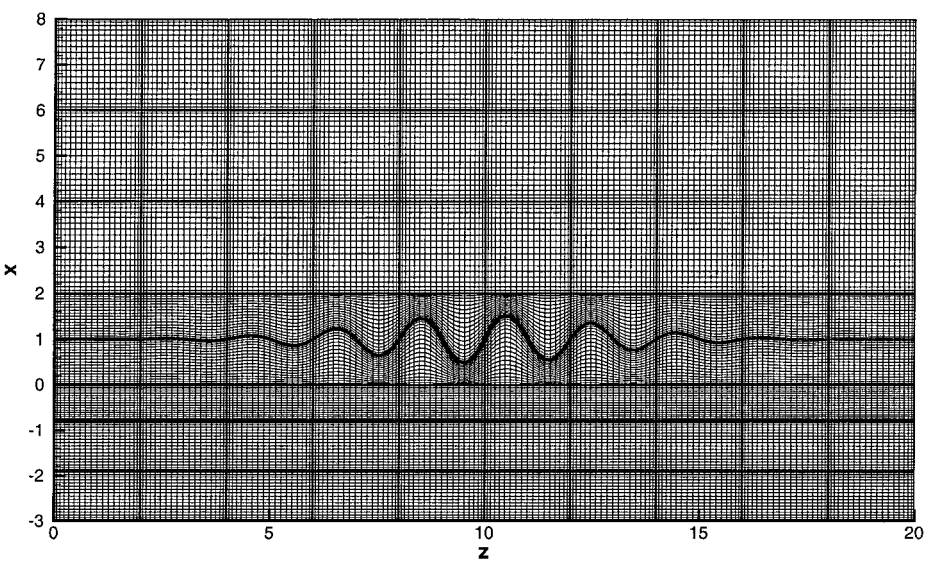

FIG. 5. Illustration of an out-of-plane waveguide coupling test case. The core layer of the waveguides is right below $x = 0$ while the absorbing layers are not shown.

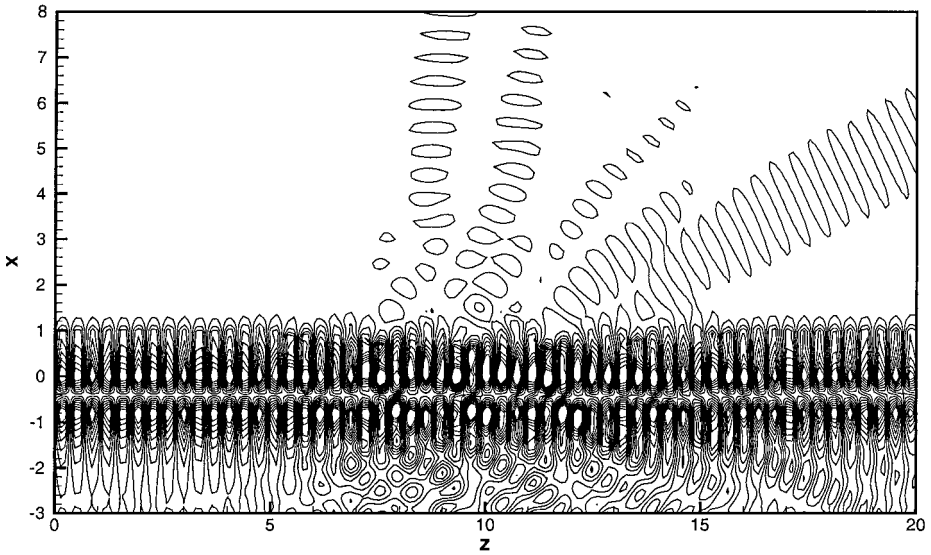

FIG. 6. The H_z field component at t = 190.

As is clear from Fig. 5, the computation domain is chosen relatively wide as compared to the width of the surface modulation. This is done to ensure that the virtual aperture used in the subsequent near- and farfield calculations captures all of the radiation from the surface-relief grating. The virtual aperture is placed at $x = 2$.

In Fig. 6 we show a snapshot of the H_z component at $t = 190$, clearly illustrating the coupling of the waveguide energy into free-space waves as a consequence of the surface modulation.

To further investigate the out-coupled light we employ the field equivalence principle discussed in Subsection 3.6. As a way of validating the transformation as well as the accuracy of the computation framework, we compare a directly computed nearfield along the line $x = 6$ with that obtained through the transformation of the phasors along $x = 2$. The results are shown in Fig. 7, where the amplitude of the H_z in its phasor representation calculated both directly and using the field equivalence principle is plotted, confirming the

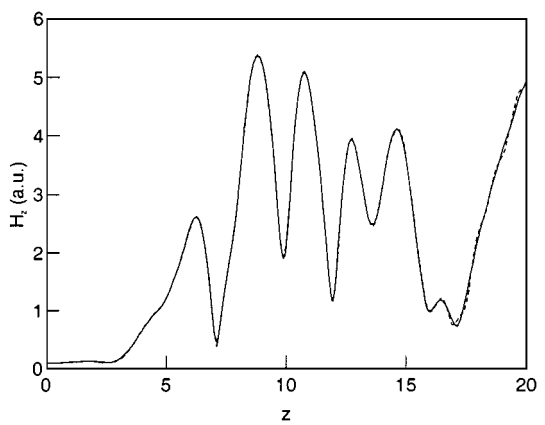

FIG. 7. Nearfield calculation using both direct calculation and calculation using field equivalence at $x = 6$. Solid line, direct solution; dashed line, solution obtained with free-space integration.

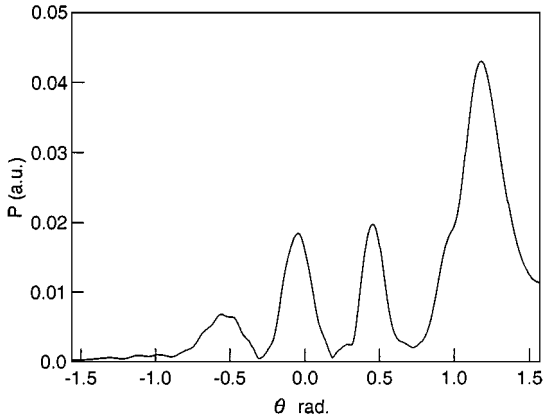

FIG. 8. θ-component of radiation integral L as a function of the observation angle, θ.

accuracy as well as the consistency of the different approaches. This also confirms that the non-closedness of the virtual contour does not represent a source of errors as long as the aperture is wide compared to the modulation of the waveguide surface.

As a final example, we calculate the farfield pattern based on the approximate expressions in Eq. (15), yielding the results shown in Fig. 8 and illustrating the output power in an arbitrary distance in the farfield as a function of the observation angle. The peaks reflects the diffraction orders of the problem.

4.4. *Parallelization Issues*

As mentioned previously the multi-domain formulation is well suited for implementation on parallel computers. We have parallelized the code on a cluster of IBM RS/6000 SP nodes connected through a high performance switch with a bandwidth of 100 Mbits/s. The code is written in Fortran 77 and has been parallelized using the message passing interface (MPI) set of libraries. Figure 9 shows the speed-up factor as a function of the number of nodes on which the execution is distributed. The test case consists of 440 domains. It is seen that the parallelization speed-up is very reasonable with a speed-up of 6.1 for 8 processors

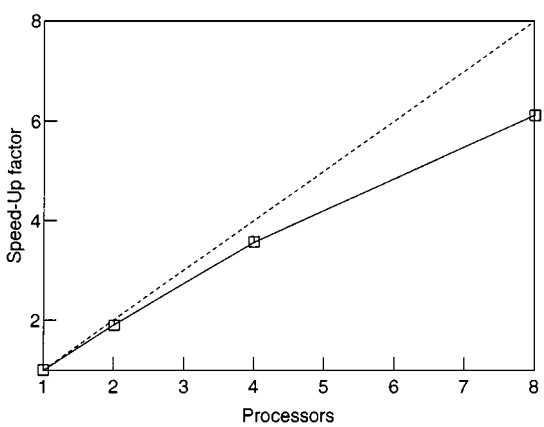

FIG. 9. Parallelization speed-up factors for a case employing 440 elements.

in parallel. This efficient parallelization is due mainly to the fact that the exchange of information between processors is limited to the fields on the borders of the subset of domains distributed to the individual processors.

5. CONCLUDING REMARKS

We have presented a parallel spectral collocation time-domain method for the accurate and efficient modeling of general waveguides with special attention being paid to the modeling of waveguide couplers with a general surface-relief grating.

Through a number of computational tests we confirmed the accuracy and robustness of the scheme for modeling wave propagation in thin film waveguides. Only 7–9 points per wavelength are necessary to accurately evolve the wavetrains, thus making way for a significant reduction in computational requirements as compared to more traditional low order methods and an enhanced ability to model electrically very large problems. The combination of the multi-domain formulation and smooth mappings yields a geometrically flexible scheme that, as we have shown, is well suited for implementation on parallel computers.

The specification of the complete scheme involves a detailed comparison of two different types of absorbing boundary conditions, PML and ML, establishing that the PML method is slightly more efficient for our purpose, and that the error introduced by using such an absorbing boundary is of the order of the approximation. Moreover, we also discussed using a singular grid-mapping, showing that it could significantly increase the maximum allowable time-step without sacrificing the spectral convergence.

Combined with the use of the field equivalence principle for near- and farfield calculations, the spectral collocation scheme provides a powerful tool for analyzing radiation from a large class of diffractive optical elements.

ACKNOWLEDGMENTS

The work of the first author (J.S.H.) was partially supported by AFOSR/DARPA Grant F49620-96-1-0426 and NSF Grant ASC-9504002. He also greatfully appreciates partial support of Risø National Laboratory for an extended visit there during which much of the described work was completed. Steen Hanson and Lars Lading are greatfully acknowledged for their stimulating input in numerous fruitful discussions. This work was supported by the Danish Research Councils.

REFERENCES

1. S. Abarbanel and D. Gottlieb, A mathematical analysis of the PML method, *J. Comput. Phys.* **134**(2), 357 (1997).
2. S. Abarbanel, D. Gottlieb, and J. S. Hesthaven, Wellposed perfectly matched layers for advective acoustics, *J. Comput. Phys.*, in press.
3. J. P. Berenger, A perfectly matched layer for the absorption of electromagnetic waves, *J. Comput. Phys.* **114**, 185 (1994).
4. M. H. Carpenter and C. A. Kennedy, *Fourth Order 2N-Storage Runge–Kutta Scheme*, Technical Report, NASA-TM-109112, 1994.
5. W. S. Don and A. Solomonoff, Accuracy enhancements for higher derivatives using chebyshev collocation and a mapping technique, *SIAM J. Sci. Comput.* **18**, 1040 (1997).

6. K. H. Dridi and A. Bjarklev, Optical electromagnetic vector-field modeling for the accurate analysis of finite diffractive structures of high complexity, *Appl. Opt.* **38**(9), 1668 (1999).
7. P. Fischer and D. Gottlieb, On the optimal number of subdomains for hyperbolic problems on parallel computers, *Int. J. Supercomput. Appl. High Perform. Comput*. **11**(1), 65 (1997).
8. D. Funaro, *Polynomial Approximation of Differential Equations*, Lecture Notes in Physics (Springer-Verlag, Berlin, 1992), Vol. 8.
9. W. J. Gordon and C. A. Hall, Transfinite element methods: Blending-function interpolation over arbitrary curved element domains, *Numer. Math*. **21**, 109 (1973).
10. B. Yang, D. Gottlieb, and J. S. Hesthaven, On the use of PML ABC's in spectral time-domain simulations of electromagnetic scattering, in *Proceedings of the 13th Annual Review of Progress in Applied Computational Electromagnetics* (Naval Postgraduate School, Monterey, CA, March 1997), Vol. II, p. 926.
11. S. G. Hanson, L. R. Lindvold, and L. Lading, A surface velocimeter based on a holographic optical element and semiconductor components, *Meas. Sci. Technol*. **7**, 69 (1996).
12. J. S. Hesthaven, A stable penalty method for the compressible Navier–Stokes equations. II. One dimensional domain decomposition schemes, *SIAM J. Sci. Comput*. **18**, 658 (1997).
13. J. S. Hesthaven, A stable penalty method for the compressible Navier–Stokes equations. III. Multi dimensional domain decomposition schemes, *SIAM J. Sci. Comput*. **20**, 62 (1999).
14. D. Kopriva, A spectral multidomain method for the solution of hyperbolic systems, *Appl. Numer. Math*. **2**, 221 (1986).
15. D. Kopriva, private communication, 1997.
16. D. Kosloff and H. Tal-Ezer, Modified Chebyshev pseudospectral methods with $O(n^{-1})$ time-step restriction, *J. Comput. Phys*. **104**(2), 457 (1993).
17. C. Canuto, M. Y. Hussaini, A. Quarteroni, and T. A. Zang, *Spectral Methods in Fluid Dynamics*, Springer Series in Computational Physics (Springer-Verlag, New York, 1987).
18. S. Ramo, J. R. Whinnery, and T. van Duzer, *Fields and Waves in Communications Electronics*, 3rd ed. (Wiley, New York, 1993).
19. R. Renaut and J. Fröhlich, A pseudospectral Chebyshev method for the 2D wave equation with domain stretching and absorbing boundary conditions, *J. Comput, Phys*. **124**, 324 (1996).
20. S. A. Schelkunoff, Some equivalence theorems of electromagnetics and their application to radiation problems, *Bell Systems Tech. J.* **15**, 92 (1936).
21. A. Taflove, *Computational Electrodynamics—The Finite-Difference Time-Domain Method* (Aztech House, Boston, 1995).
22. S. Ura, Y. Furrukawa, T. Suhara, and H. Nishihara, Linearly focusing grating coupler for integrated-optic parallel pickup, *J. Opt. Soc. Am. A* **7**, 1759 (1990).
23. B. Yang, D. Gottlieb, and J. S. Hesthaven, Spectral simulation of electromagnetic wave scattering, *J. Comput. Phys*. **134**, 216 (1997).